



Article

Fe₃C-Decorated Folic Acid-Derived Graphene-like Carbon-Modified Separator as a Polysulfide Barrier for High-Performance Lithium-Sulfur Batteries

Zenghui Lin [†], Junan Feng [†], Wendong Liu, Lu Yin, Wanyang Chen, Chuan Shi and Jianjun Song ^{*}

College of Physics, Qingdao University, Qingdao 266071, China

^{*} Correspondence: jianjun.song@qdu.edu.cn[†] These authors contributed equally to this work.

Abstract: The lithium-sulfur (Li-S) battery has been regarded as an important candidate for the next-generation energy storage system due to its high theoretical capacity (1675 mAh g^{-1}) and high energy density (2600 Wh kg^{-1}). However, the shuttle effect of polysulfide seriously affects the cycling stability of the Li-S battery. Here, a novel Fe₃C-decorated folic acid-derived graphene-like N-doped carbon sheet (Fe₃C@N-CS) was successfully prepared as the polysulfide catalyst to modify the separator of Li-S batteries. The porous layered structures can successfully capture polysulfide as a physical barrier and the encapsulated Fe₃C catalyst can effectively trap and catalyze the conversion of polysulfide, thus accelerating the redox reaction kinetics. Together with the highly conductive networks, a cell with the Fe₃C@N-CS-modified separator evinces superior cycling stability with 0.06% capacity decay per cycle at 1 C rate over 500 cycles and excellent specific capacity with an initial capacity of 1260 mAh g^{-1} at 0.2 C. Furthermore, at a high sulfur loading of 4.0 mg cm^{-2} , the batteries also express superb cycle stability and rate performance.



Citation: Lin, Z.; Feng, J.; Liu, W.; Yin, L.; Chen, W.; Shi, C.; Song, J. Fe₃C-Decorated Folic Acid-Derived Graphene-like Carbon-Modified Separator as a Polysulfide Barrier for High-Performance Lithium-Sulfur Batteries. *Batteries* **2023**, *9*, 296. <https://doi.org/10.3390/batteries9060296>

Academic Editors: Carlos Ziebert and Changshin Jo

Received: 28 March 2023

Revised: 20 May 2023

Accepted: 28 May 2023

Published: 29 May 2023



Copyright: © 2023 by the authors. Licensee MDPI, Basel, Switzerland. This article is an open access article distributed under the terms and conditions of the Creative Commons Attribution (CC BY) license (<https://creativecommons.org/licenses/by/4.0/>).

Keywords: lithium-sulfur batteries; Fe₃C; 2D materials; shuttle effect; catalyst

1. Introduction

The development of modern energy storage systems is undoubtedly a consequential part of the implementation of carbon-neutral strategies in response to the current environmental situation. Lithium-sulfur (Li-S) batteries are one of the most promising candidates due to their high energy density (2600 Wh kg^{-1}) and high theoretical capacity (1675 mAh g^{-1}) [1,2]. Additionally, sulfur is extremely rich in the earth, nonpoisonous, and eco-friendly [3]. Nevertheless, there are still obstructions to practical commercial application: (i) Sulfur and Li₂S have poor electrical conductivity and the insulating properties make it more difficult to transport ions and electrons. (ii) The cathode will be seriously damaged by the significant volume expansion due to the density difference between sulfur and Li₂S. (iii) The intermediate polysulfides (LiPSs) dissolving in the organic electrolyte will shuttle between the anode and cathode during the reaction process, and this undesirable shuttle effect is not conducive to the full utilization of active material sulfur [4]. Moreover, the sluggish conversion kinetics between the interface redox kinetics from LiPSs to Li₂S results in a disappointing decay rate of capacity and electrochemical polarization [5].

To solve the above problems, most research has focused on the design of the functional sulfur host [6,7], appropriate separator modification [8,9], and electrolyte optimization [10,11]. Among them, the modification of separators is a facile strategy to seek a good cycle lifespan of Li-S batteries, and the ideal separators can effectively fix LiPSs on the side of the cathode to prevent them from reacting with the lithium anode [12,13]. Simultaneously, the functional layer can also serve as the second current collector to ensure the fast transmission of electrons and act as a storage for LiPSs. Among the various adjustments made to the separator, carbon materials are a major focus due to the high

electrical conductivity and the enhanced wettability of electrolytes [14]. Carbon materials, such as conductive carbon nanotubes (CNTs) [15], porous carbon, and carbon nanofibers (CNFs) [16], can effectively reduce the internal interface impedance and charge transfer resistance, improving the Li^+ diffusion kinetics [17]. However, a single non-polar carbon-material-modified separator cannot fully inhibit the shuttle effect relying solely on weak physical adsorption or electrostatic interaction [18,19]. Polar materials, such as transition metal compounds, produce robust polar chemical interaction on LiPSs and can catalyze the conversion of LiPSs to increase the reaction kinetics of Li-S chemistry [20]. Therefore, the reasonable combination of polar metal oxides, carbides, nitrides, and sulfides with carbon-based materials has shown outstanding properties and has become a popular choice in the field of sulfur host design or separator modification of Li-S batteries [21–25]. Fe_3C , with the advantages of low price, simple preparation, high conductivity, strong polarity, and remarkable electrochemical catalysis ability make it excellent in the field of LiPSs catalysis. Li et al. synthesized a Janus electrode comprising Fe_3C nanoparticles as active catalytic sites, and the electrode displayed a synergistic dual adsorption–electrocatalysis function, which can assuage the shuttle effect by facilitating the kinetics of redox reactions from the soluble LiPSs to the insoluble LiPSs efficiently [26–28].

Two-dimensional (2D) materials, such as graphene (GN) and MXene, are seen as a high-quality options for electrochemical energy storage study [29–33], due to excellent ductility, high specific surface area, and exceptional electrical conductivity [34]. Moreover, the unique 2D structure can not only provide a great quantity of ion transport channels in the electrochemical kinetics process, but also act as a physical barrier for LiPSs. To achieve the efficient catalytic effect, carbon material as the base which can realize the platform of uniform catalyst loading is an important guarantee [34]. Although the 2D material graphene is an excellent carrier for catalysts, the more complicated preparation technology greatly limits its application prospect as carbon support material. Therefore, it will be highly promising to find a facile approach to compound Fe_3C with the 2D material GN to achieve the dual physical/chemical adsorption of polysulfide and enhanced redox reaction kinetics.

In this work, we prepared a novel Fe_3C -decorated folic acid-derived GN-like N-doped carbon sheet ($\text{Fe}_3\text{C}@\text{N-CS}$) as the LiPSs catalyst to modify the separator of Li-S batteries. After the hydrothermal method, freeze-drying, and calcination process, the folic acid produced a GN-like structure with interconnected porous lamellar structures with high specific surface area to ensure generous ion migration channels [35] (Figure 1). More importantly, the barrier produced by self-inter-stacking can also serve as a physical barrier to enhance the efficiency of LiPSs capture. The well-dispersed polar Fe_3C nanoparticles on the nanosheet assure abundant chemical adsorption and active catalytic sites to enhance the reaction kinetics of the LiPSs by catalyzing the redox conversion. Profiting from the synergy efficiency of chemisorption and catalytic properties of Fe_3C and the physisorption of highly conductive 2D carbon nanosheets, the Li-S batteries with $\text{Fe}_3\text{C}@\text{N-CS}$ -modified separators demonstrated brilliant specific capacity with an excellent capacity of 1260 mAh g^{-1} at 0.2 C and outstanding cycling stability with 0.06% capacity decay per cycle at 1 C over 500 cycles. Even at a high sulfur loading of 4.0 mg cm^{-2} , the batteries still accomplish exceptional cycle stability and rate performance.

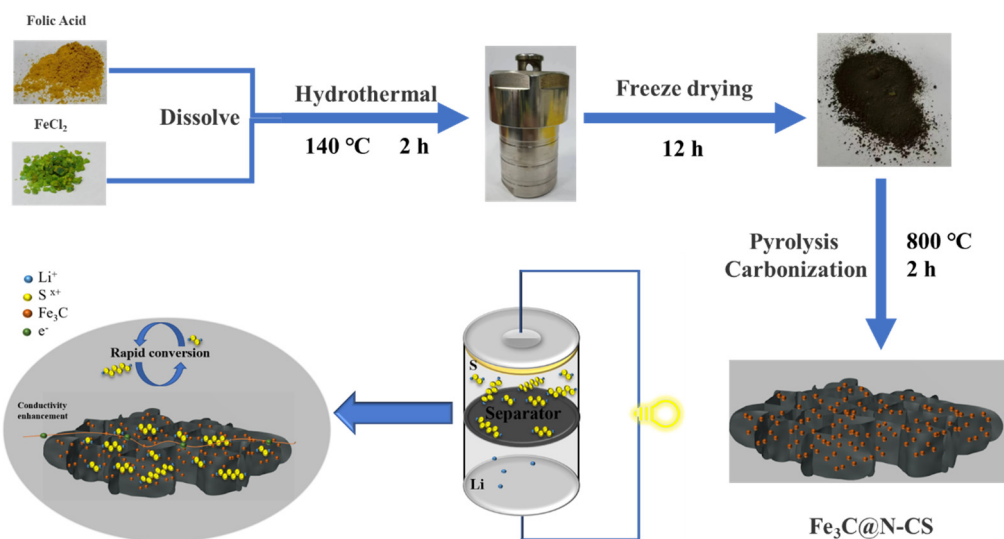


Figure 1. Schematic diagram illustration of the fabrication process of $\text{Fe}_3\text{C}@\text{N-CS}$ and the LiPSs conversion process on the surface of $\text{Fe}_3\text{C}@\text{N-CS}$.

2. Materials and Methods

2.1. Preparation of $\text{Fe}_3\text{C}@\text{N-CS}$ Carbon Sheet

Typically, $\text{FeCl}_2 \cdot 4\text{H}_2\text{O}$ (200 mg) and folic acid (220 mg) were dissolved into a mixture of deionized water (5.5 mL) and anhydrous ethanol (8 mL). Then, the mixed solution was transferred to the autoclave for a solvothermal reaction at a temperature of 140°C for two hours. Afterward, the solution was centrifuged with deionized water three times and freeze-dried for ten hours after being frozen overnight. The dried precursor powder was placed in a ceramic boat held in an argon-filled tube furnace and heated to 800°C with a heating rate of 5°C min^{-1} and then held for 2 h to obtain a black powder, marked as $\text{Fe}_3\text{C}@\text{N-CS}$. N-CS was produced by the same process but without the addition of the Fe source.

2.2. Fabrication of $\text{Fe}_3\text{C}@\text{N-CS}$ -Coated Separator

A homogenous slurry consisting of $\text{Fe}_3\text{C}@\text{N-CS}$ and polyvinylidene difluoride (PVDF) with a mass ratio of 5:1 in N-methyl-2-pyrrolidone solvent was uniformly pasted onto the standard PP separator and dried under vacuum at 60°C for 12 h. The thickness of the modified diaphragm was approximately $7.63\text{ }\mu\text{m}$. The separator was cut into discs with a diameter of 19 mm.

2.3. Synthesis of Lithium Li_2S_6 Solution

Li_2S_6 solution was prepared by adding Li_2S and S powders into the solvent containing 1,2-dimethoxyethane and 1,3-dioxolane with a volume ratio of 1:1 and vigorously stirred for 48 h in the glovebox at 60°C . The molar ratio of Li_2S and S was 1:5.

2.4. Preparation of Cathodes

The mixture of sulfur and Ketjen Black was fully mixed and then heated to 155°C and maintained for 12 h. Through thermogravimetric analysis (TGA), the sulfur content was about 75.43 wt% (Figure S1). The slurry of KB/S compounds, Ketjen Black, and polyvinylidene difluoride (PVDF) with a ratio of 8:1:1 (namely the sulfur content in the total S electrode consisting of binder and the conductive agent was about 60 wt%) in the solvent of N-methyl-2-pyrrolidone (NMP) was coated on conductive aluminum foil. As determined by weighing and calculating, the sulfur loading in each cathode was about 1.2 mg cm^{-2} .

2.5. Electrochemical Measures

CR-2032-type coin cells were assembled with a sulfur cathode, modified separator, electrolyte, and lithium anode in a glovebox under an argon atmosphere ($H_2O \leq 0.01$ ppm, $O_2 \leq 0.01$ ppm). The electrolyte was 1 M lithium bis(trifluoromethane sulfonimide) (LiTFSI) in a mixed solvent of DME/DOL (1: 1, *v/v*) with 0.1 M LiNO₃ as additives. The electrochemical workstation (CHI 760e) was applied to analyze cyclic voltammetry (CV) curves at a working voltage from 1.7 to 2.8 V and a scan rate of 0.1~0.6 mV s⁻¹. Electrochemical impedance spectroscopy (EIS) measurements were tested at 1 mHz to 100 kHz and applied amplitude of 5 mV. The electrochemical information was reported on the NEWARE battery measurement system at indoor temperature, and the voltage range was 1.7~2.8 V.

2.6. Material Characterization

XRD (Cu Ka radiation with $k = 1.5405$ Å) was conducted to investigate the phase information of materials in the angle range of 5° to 80°. The SEM (Nova Nano SEM450, 15K eV) and the structure and morphologies of the materials were analyzed with TEM (JEOL JEM 2100F). The XPS was used on ESCALAB250 to detect the chemical composition of samples. HRTEM and attached EDS equipment (Oxford Instruments and EDAX) were employed to analyze the structure and elemental distribution of the materials. The ultraviolet/visible absorption (UV-vis) spectra were measured using a UV-vis variable wavelength spectrophotometer (AUTOLAB). TGA was used to measure the content of substances at different temperature intervals and under different atmospheres (ME204E/02).

3. Results and Discussion

The microstructure of samples was observed with a scanning electron microscope (SEM). The raw folic acid without heat treatment showed a micron-scale caked structure (Figure S2). After calcination, the folic acid-derived N-CS exhibited two-dimensional carbon nanosheet characteristics as well as GN-like layering and wrinkle structure (Figure 2a and Figure S3). The SEM images of Fe₃C@N-CS (Figure 2b,c) demonstrate that the crinkled and lamellar microstructure was perfectly inherited, and the surface of the lamellar sheet became rougher. At the same observation scale, the Fe₃C@N-CS lamellar structure with a unique interconnected porous structure provided more active site exposure as well as an increased contact interface with LiPSs (Figure S4). The difference between Fe₃C@N-CS and N-CS in microstructure is mainly attributed to the introduction of iron carbide into crystallization and the graphitization of carbon during the formation process of Fe₃C. Fe²⁺ and folic acid form the precursor of supramolecular assemblies in the pyrolysis process, which catalyzes the graphitization of the carbon matrix to form more pores in the subsequent high-temperature carbonization process [36].

The transmission electron microscope (TEM) images (Figure 2d,e) also reveal the typically GN-like unilateral and wrinkle-layered structure of Fe₃C@N-CS, which offers rich channels for ion migration. (Figure S4). The lattice spacing of 0.47 nm was measured under high-resolution TEM (HRTEM), which corresponds to the (001) crystal plane of Fe₃C (Figure 2f). The circled part shows the graphitized lattice streaks of carbon catalyzed by Fe at high temperatures [37,38]. The high-angle annular dark field SEM (STEM-HAADF) image and EDS mapping of Fe₃C@N-CS (Figure 2g) show that the folding characteristics of the signal-layer two-dimensional structure and the uniform distribution of the characteristic elements (Fe, O, N, C) constituting the Fe₃C@N-CS. The nitrogen atoms in folic acid molecules were carbonized to achieve nitrogen doping of Fe₃C@N-CS. X-ray diffractometer (XRD) characterization results revealed the material composition of Fe₃C@N-CS and N-CS (Figure 3a).

The diffraction peaks of as-prepared Fe₃C were almost in agreement with Fe₃C (PDF#85-0871), demonstrating the successful synthesis of Fe₃C [26]. Solvothermal promotes the dissociation and dissolution of folic acid with Fe³⁺ to form combinations that are calcined to Fe₃C during subsequent carbonization. The TGA test was conducted to detect the Fe₃C content in the sample under an air atmosphere (Figure 3b). The first stage

of mass loss is the loss of surface adsorbed water, and the second stage is the oxidation process of carbon at high temperatures. The results showed that the Fe₃C content of the prepared sample was 4.5%. Through Raman spectroscopy study of the material (Figure 3c), the Fe₃C@N-CS showed a higher degree of graphitization (A_D/A_G value of 1.552) than that of N-CS (A_D/A_G value of 1.758) owing to the introduction of Fe₃C. In the cross-sectional SEM image (Figure 3d), the Fe₃C@N-CS-modified separator shows that the thickness of the Fe₃C@N-CS functional layer was about 7.63 μm , and the average mass loading on each separator was only 0.16 mg cm⁻², which is beneficial to improve the mass–energy density of the battery. The contact angle test (Figure 3e) was used to evaluate the wetting condition of the different separators to the electrolyte. After dropping the electrolyte for 5 s, the electrolyte permeated quickly into the Fe₃C@N-CS-modified separator, and the contact angle was about $\theta = 2.48^\circ$. In comparison, the traditional PP separator showed a contact angle of $\theta = 48.48^\circ$. The excellent hydrophilic property allows fast ion diffusion across the Fe₃C@N-CS-modified separator. Figure 3f shows that the Fe₃C@N-CS-modified separator can restore the original shape without the slag phenomenon after folding, which shows good flexibility for practical application.

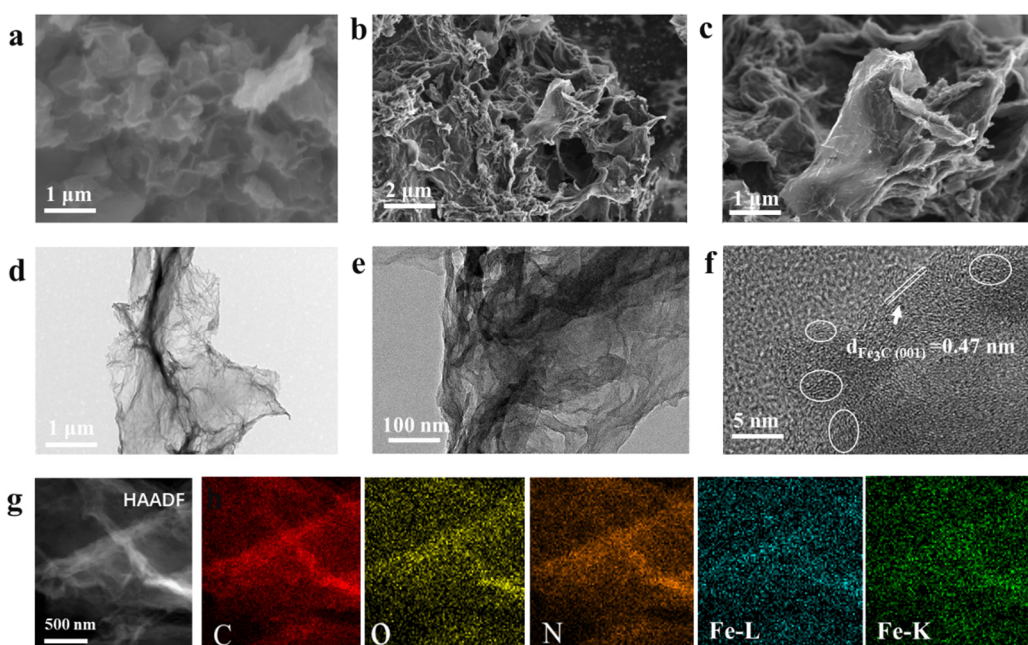


Figure 2. SEM images of N-CS (a) and Fe₃C@N-CS (b,c). TEM images of Fe₃C@N-CS (d,e). HR-TEM image of Fe₃C@N-CS (f). STEM-HADDF of Fe₃C@N-CS and elemental mapping images of C, O, N, Fe-L, and Fe-K in a selected region of Fe₃C@N-CS (g).

X-ray photoelectron spectrometer (XPS) analyses were carried out to measure the chemical state and composition of samples. Figure S5 shows that the Fe₃C@N-CS consisted of Fe, O, N, and C. In the HRXPS spectra of Fe 2p, there were four peaks (Figure 4a) which could be distinguished at 709.3 eV, 714.04 eV, 722.2 eV, and 725.92 eV. The four peaks can be assigned to Fe²⁺ and Fe³⁺ [26]. In the C 1s HRXPS spectrum of Fe₃C@N-CS (Figure 4b), the peaks corresponding to C=C/C–C, C, C–N, and -C=O bonds were observed at 283.08 eV, 284.23 eV, 286.78 eV, and 290.08 eV, respectively [39]. The presence of C–N bond indicates the successful doping of nitrogen in carbon. The N 1s HRXPS spectrum could be fitted to four components corresponding to pyrrole-N (397.33 eV), pyridine-N (396.58 eV), graphite-N (399.28 eV), and C–N (402.84 eV) (Figure 4c) [40], and the content of pyridinic, pyrrolic, graphitic, and C–N was calculated to be 20.9%, 20.8%, 44.2%, and 13.9%, respectively. In the O 1s HRXPS spectrum (Figure 4d), oxygen vacancy, lattice oxygen, and hydroxyls species were detected at 531.53 eV, 530.63 eV, and 529.43 eV, respectively [40]. The abundant oxygen

vacancies can provide active sites during redox reactions, which is beneficial for anchoring and conversion of LiPSs.

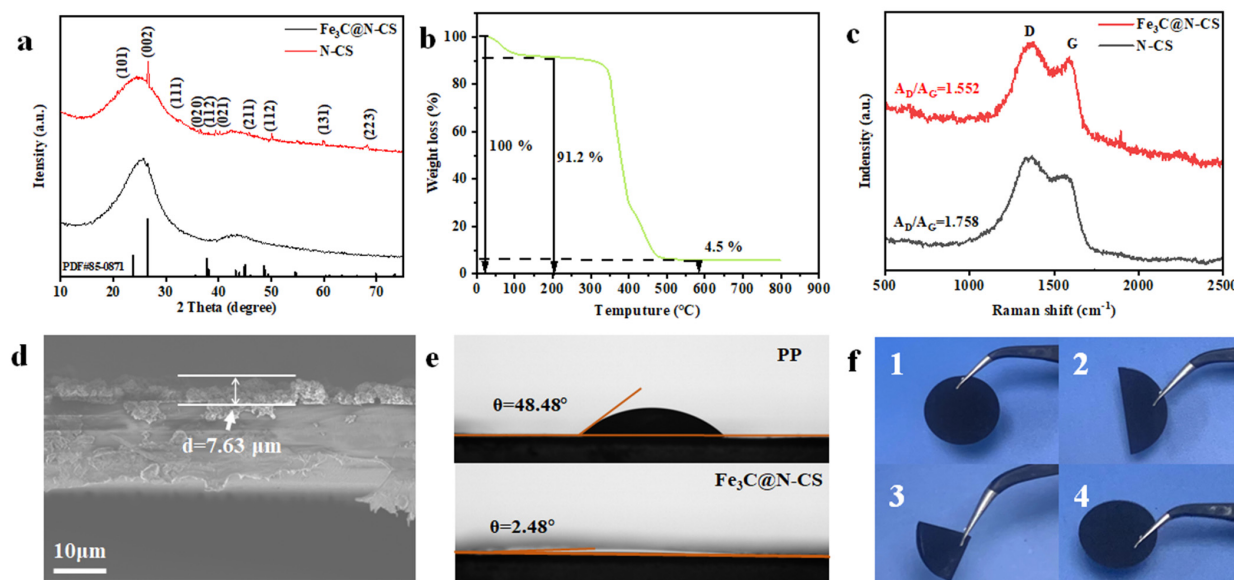


Figure 3. The XRD patterns of N-CS and Fe₃C@N-CS (a). The TGA curve (b) and Raman spectra (c) of Fe₃C@N-CS. Cross-section SEM image of Fe₃C@N-CS-modified separator (d). Contact angle test between separator and electrolyte of Fe₃C@N-CS-modified separator and PP separator (e). The flexibility test of Fe₃C@N-CS-modified separator (f).

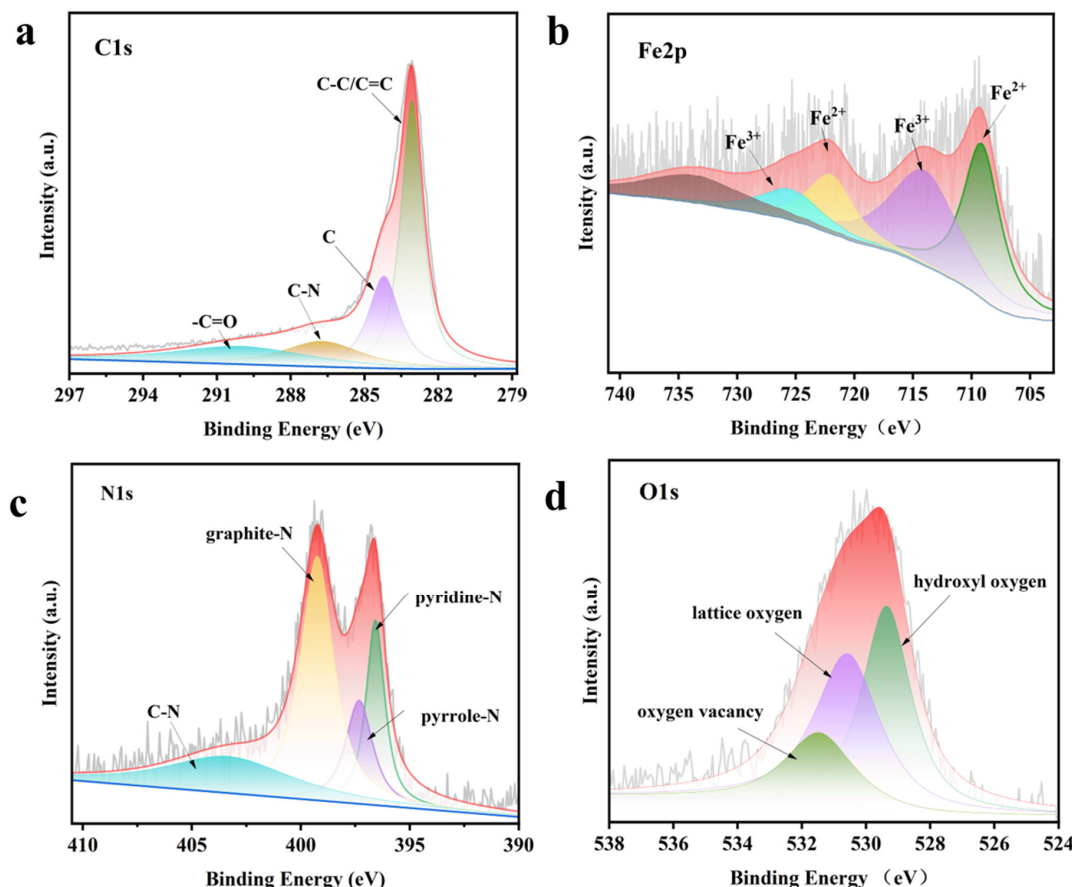


Figure 4. The XPS spectra of Fe₃C@N-CS of Fe 2p (a), C 1s (b), N 1s (c), and O 1s (d).

To evaluate the effect of the $\text{Fe}_3\text{C}@\text{N-CS}$ -modified separator on the electrochemical performance of Li-S batteries, simple S/CB composites were used as sulfur cathode materials to estimate the electrochemical performance. As shown in Figure 5a, the cycle performance at 0.2 C ($1 \text{ C} = 1675 \text{ mA g}^{-1}$) showed that the cell with the $\text{Fe}_3\text{C}@\text{N-CS}$ -modified separator delivered a high initial discharge capacity of 1260 mAh g^{-1} , which coincides with 75.2% of the theoretical capacity of sulfur, which shows much more stable performance than the cells with the N-CS-modified-separator and PP separator. The galvanostatic charge/discharge curves in Figure 5b show that the cell with the $\text{Fe}_3\text{C}@\text{N-CS}$ -modified separator possessed longer plateaus and lower overpotential (ΔE) than others, proving the reduced electrochemical polarization and the rapid reaction kinetics of LiPSs. At 1 C (Figure 5c), the cycle performance of the cell with the $\text{Fe}_3\text{C}@\text{N-CS}$ -modified separator was still prominent, compared with the cells with the N-CS-modified separator and normal PP separator. For the long-term cycle of 1 C (Figure S6), the initial capacity of the cell with the $\text{Fe}_3\text{C}@\text{N-CS}$ -modified separator exhibited excellent cycling performance with a high capacity of 890 mA h g^{-1} and low average capacity decay rate per cycle of only 0.06% after 500 cycles.

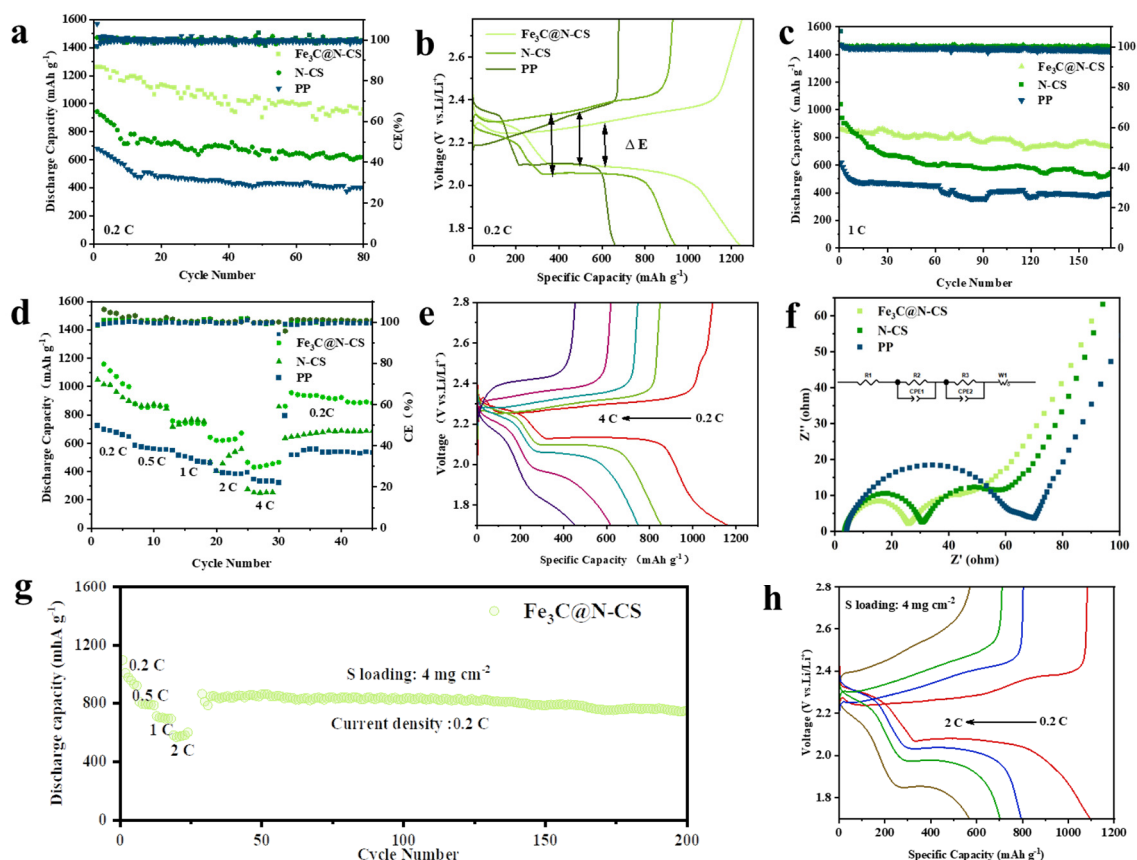


Figure 5. Cycling performance of the cells with $\text{Fe}_3\text{C}@\text{N-CS}$ -modified separator, N-CS-modified separator, and PP separator at 0.2 C (a). Galvanostatic discharge/charge profiles of the cells with $\text{Fe}_3\text{C}@\text{N-CS}$ -modified separator, N-CS-modified separator, and PP separator at 0.2 C (b). The cycling performance of the cells with different separators at 1 C (c). The rate performance of the cells with different separators (d) and the charge–discharge profiles of the Li-S batteries with $\text{Fe}_3\text{C}@\text{N-CS}$ -modified separator (e). The EIS spectra of the cells with different separators before the charge/discharge cycling (f). Rate performance of Li-S batteries with $\text{Fe}_3\text{C}@\text{N-CS}$ -modified separator under high S loading of 4 mg cm^{-2} (g) and its charge/discharge curves (h).

The cycle stability of the batteries is revealed by the slight changes in the charging and discharging platform of the galvanostatic charge-discharge curve at 1 C for 500 cycles

(Figure S7a). The rate performance (Figure 5d) of the cells with various separators showed that the cell with the Fe₃C@N-CS-modified separator delivered higher reversible specific capacities of 1158.93, 878.1, 757.7, 641.7, and 464.86 mAh g⁻¹ at 0.2, 0.5, 1, 2, and 4 C, respectively, than those using the N-CS and PP separator, which can be attributed to the excellent catalytic effect of Fe₃C and rich defect sites caused by N doping. The charge-discharge curves at different rates are also significant for evaluating the effect of Fe₃C@N-CS on reducing activation energy and enhancing the electrochemical performance of LiPSs. Subsequently, the galvanostatic charge/discharge curves of the initial cycle from 0.2 C to 4 C are displayed (Figure 5e); with the increase in current density, the polarization potential increases gradually, even up to a high current density of 4 C, two typical discharge platforms can also be maintained, indicating the effective transformation of sulfur species. Figure 5f and Figure S8 show the electrochemical impedance spectroscopy (EIS) of cells with different separators before and after 50 cycles at 1 C, and the fitting profiles consisted of two semicircles and a slope line corresponding to the charge transfer resistance (R_{ct}), interface resistance (R_f), and the Warburg impedance, respectively. As expected, the R_{ct} in both EIS spectra before (~21 Ω) or after (~5 Ω) cycling of the cell with the Fe₃C@N-CS-modified separator was lower than that of the PP (~56/15 Ω) and N-CS (~26/7 Ω) separators owing to the abundant electron migration channels provided by the highly graphitized 2D conductive plane produced by the catalytic action of iron [41].

To evaluate the potential of practicality, high sulfur loading cycle performance is the stepping stone. The rate performance of the cells with the Fe₃C@N-CS-modified separator under high sulfur loading of 4 mg cm⁻² was evaluated and shown in Figure 5g,h. Under the condition of high sulfur load and high current density, a relatively regular charging and discharging platform was still maintained. The cell with the Fe₃C@N-CS-modified separator still exhibited the reversible capacity of 1095.8, 809.31, 713.22, 582.33, and 864.79 mAh g⁻¹ at 0.2 C, 0.5 C, 1 C, 2 C, and back to 0.2 C, respectively, which indicates good performance on the redox reaction of LiPSs of Fe₃C particles and the enhancement of electrochemical reaction kinetics. After the rate performance test, the cell was cycled at 0.2 C to 200 cycles; the galvanostatic discharge/charge profiles of the cell with the Fe₃C@N-CS-modified separator under high S loading of 4 mg cm⁻² showed an obvious plateau and ΔE did not change (Figure S7b), which shows its strong inhibition ability for the shuttle effect of Fe₃C@N-CS.

This demonstrates that the cooperative effect of physical and chemical adsorption can effectively alleviate the shuttle effect under a high sulfur loading state, and thus heighten the utilization rate of sulfur-active materials. In comparison with the electrochemical performance shown in Table S1, the performance of this work is quite outstanding.

In the cyclic voltammetry (CV) curves (Figure 6a), for the cathodic scan, the first peak at 2.67 V, corresponds to the transformation of ring-opening reduction S₈ to soluble long-chain Li₂S_x (4 ≤ x ≤ 8). The second peak at 2.01 V corresponds to the reduction of Li₂S_x (4 ≤ x ≤ 8) to the short chain Li₂S₂/Li₂S. Subsequently, in the anodic scan, the implication of the oxidation peak at 2.36 V represents that the short-chain Li₂S/Li₂S₂ is oxidized to the long-chain LiPSs further Li₈S/S [42]. The cell with the Fe₃C@N-CS-modified separator showed a higher current response density than the cells with the N-CS-modified separator or PP. The same phenomenon was obtained at other different scanning rates (Figure S9), proving the positive effect of Fe₃C@N-CS on accelerating the redox kinetics. The lithium ions diffusion coefficient of batteries was also evaluated. Linear fitting was performed for the square root of each peak current and sweep rate at different sweep speeds in the measured CV curve (Figure S10). The Randles–Sevcik equation

$$I_p = \left(2.69 \times 10^5\right) \cdot C_{Li+} \cdot S \cdot n^{1.5} \cdot D_{Li+}^{1.5} \cdot v^{0.5} \quad (1)$$

can be applied to elaborate the diffusion process of lithium ions. The fitted slope ($I_p/v^{0.5}$) represents the diffusion capacity of Li⁺ [43]. The fitting results showed that the cell with the Fe₃C@N-CS-modified separator had the largest slope value compared to the others; the

reason is attributed to the significantly enhanced reaction kinetics and rich ion migration channel of the GN-like carbon nanosheet. To verify the ability of $\text{Fe}_3\text{C}@\text{N-CS}$ to catalyze the LiPSs redox reaction, the symmetric cells were tested, as shown in Figure 6b. The cells with the $\text{Fe}_3\text{C}@\text{N-CS}$ -modified separator showed a higher reversibility redox current response, and a smaller potential difference between oxidation peak and reduction peak, which indicate that $\text{Fe}_3\text{C}@\text{N-CS}$ has stronger catalytic activity than N-CS, thus accelerating the conversion kinetics of sulfur species. The ability to adsorb LiPSs was also evaluated through the visual tests of polysulfide adsorption and UV-vis spectroscopy study. Different samples with the same mass (30 mg) were dispersed in Li_2S_6 solution, and the supernatant was removed for a UV-vis test (Figure 6c). In the visual adsorption experiment, the color faded most quickly in the bottle with $\text{Fe}_3\text{C}@\text{N-CS}$, showing its excellent adsorption capacity for LiPSs. The UV-vis spectrum of the supernatant after adsorption of the bottle with $\text{Fe}_3\text{C}@\text{N-CS}$ also showed the weakest curve strength, which proved its adsorption and catalytic ability of $\text{Fe}_3\text{C}@\text{N-CS}$.

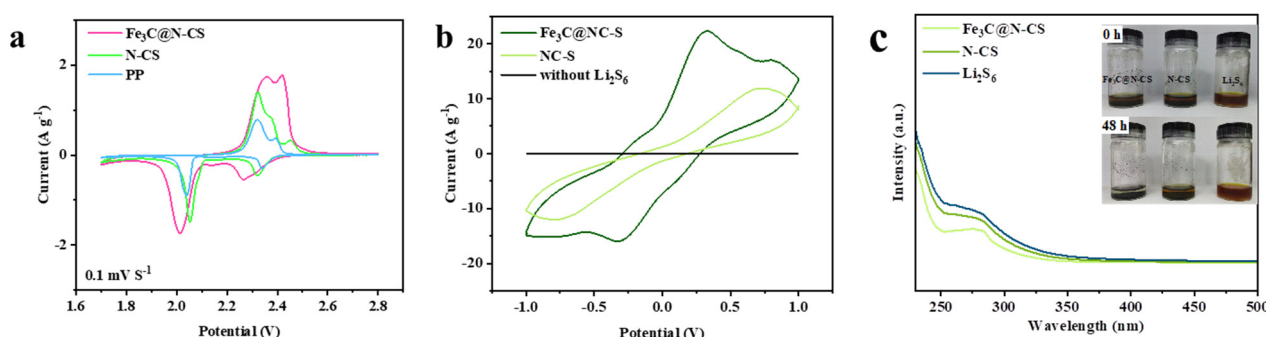


Figure 6. The CV curves of Li-S batteries with $\text{Fe}_3\text{C}@\text{N-CS}$ -modified separator, N-CS-modified separator, and PP separator at 0.1 mV s^{-1} (a). CV curves of the Li_2S_6 -symmetric cells with different samples at 10 mV s^{-1} (b). UV-vis spectra after adsorption (c).

4. Conclusions

In summary, we successfully synthesized novel Fe_3C nanoparticles-decorated folic acid-derived GN-like N-doped carbon sheet ($\text{Fe}_3\text{C}@\text{N-CS}$) composites by a simple hydrothermal method combined with the freeze-drying and annealing process. The $\text{Fe}_3\text{C}@\text{N-CS}$ shows a layered structure with abundant folds and abundant adsorption catalytic sites. The shuttling LiPSs can be adsorbed by a strongly physical interaction, and the Fe_3C can in situ catalyze the redox reaction of LiPSs. Benefiting from the physical and chemical adsorption effect and active catalytic ability of $\text{Fe}_3\text{C}@\text{N-CS}$, cells with $\text{Fe}_3\text{C}@\text{N-CS}$ separators demonstrate excellent electrochemical performance. This work provides a basis for the research of Li-S batteries based on folic acid-derived carbon and metal compounds and plays a vital role in improving the cycle stability of Li-S batteries.

Supplementary Materials: The following supporting information can be downloaded at: <https://www.mdpi.com/article/10.3390/batteries9060296/s1>; Figure S1: TGA curves for KB/S; Figure S2: SEM images of folic acid; Figure S3: SEM images of N-CS; Figure S4: SEM images of $\text{Fe}_3\text{C}@\text{N-CS}$; Figure S5: XPS spectrum of $\text{Fe}_3\text{C}@\text{N-CS}$; Figure S6: Long cycle performance of Li-S battery with $\text{Fe}_3\text{C}@\text{N-CS}$ -modified separator at 1 C; Figure S7: Galvanostatic charge/discharge profiles of Li-S battery with $\text{Fe}_3\text{C}@\text{N-CS}$ -modified separator at 1 C; Figure S8: The EIS spectra of the cells with different separators after 50 cycles at 1 C. Figure S9: CV curves of Li-S battery with $\text{Fe}_3\text{C}@\text{N-CS}$, N-CS, and PP separators at 0.2 mV s^{-1} (a), 0.4 mV s^{-1} (b), and 0.6 mV s^{-1} (c); Figure S10: CV curves of cells with $\text{Fe}_3\text{C}@\text{N-CS}$ (a), N-CS (b), PP (c) separators at $0.1\text{--}0.6 \text{ mV s}^{-1}$, and slope images of fitting linear curves of the peak currents versus square roots of scan rate (d,e,f). Table S1. Performance comparison between this work and relevant previous research [44–50].

Author Contributions: Conceptualization, data curation, formal analysis, and writing—original draft, Z.L. and J.F.; investigation, resources, data curation, W.L., L.Y., W.C. and C.S.; conceptualization,

writing—review and editing, supervision, and funding acquisition, J.S. All authors have read and agreed to the published version of the manuscript.

Funding: This research was funded by the Natural Science Foundation of Shandong Province, China (No. ZR2021QE192).

Data Availability Statement: The data are available upon reasonable request from the corresponding author.

Conflicts of Interest: The authors declare no conflict of interest.

References

- Manthiram, A.; Fu, Y.; Chung, S.-H.; Zu, C.; Su, Y.-S. Rechargeable Lithium–Sulfur Batteries. *Chem. Rev.* **2014**, *114*, 11751–11787. [\[CrossRef\]](#)
- Yan, J.; Liu, X.; Li, B. Capacity Fade Analysis of Sulfur Cathodes in Lithium–Sulfur Batteries. *Adv. Sci.* **2016**, *3*, 1600101. [\[CrossRef\]](#)
- Liang, X.; Hart, C.; Pang, Q.; Garsuch, A.; Weiss, T.; Nazar, L.F. A highly efficient polysulfide mediator for lithium–sulfur batteries. *Nat. Commun.* **2015**, *6*, 5682. [\[CrossRef\]](#)
- Bhargav, A.; He, J.; Gupta, A.; Manthiram, A. Lithium-Sulfur Batteries: Attaining the Critical Metrics. *Joule* **2020**, *4*, 285–291. [\[CrossRef\]](#)
- Jiang, F.-N.; Yang, S.-J.; Chen, Z.-X.; Liu, H.; Yuan, H.; Liu, L.; Huang, J.-Q.; Cheng, X.-B.; Zhang, Q. Higher-order polysulfides induced thermal runaway for 1.0 Ah lithium sulfur pouch cells. *Particuology* **2023**, *79*, 10–17. [\[CrossRef\]](#)
- Wang, S.-M.; Li, H.-N.; Zhao, G.-F.; Xu, L.-F.; Liu, D.-L.; Sun, Y.-J.; Guo, H. Ni₃FeN anchored on porous carbon as electrocatalyst for advanced Li–S batteries. *Rare Met.* **2022**, *42*, 515–524. [\[CrossRef\]](#)
- Tan, K.; Liu, Y.; Tan, Z.; Zhang, J.; Hou, L.; Yuan, C. High-yield and in situ fabrication of high-content nitrogen-doped graphene nanoribbons@Co/CoOOH as an integrated sulfur host towards Li–S batteries. *J. Mater. Chem. A* **2020**, *8*, 3048–3059. [\[CrossRef\]](#)
- Pang, Y.; Wei, J.-S.; Wang, Y.; Xia, Y. Synergetic Protective Effect of the Ultralight MWCNTs/NCQDs Modified Separator for Highly Stable Lithium–Sulfur Batteries. *Adv. Energy Mater.* **2018**, *8*, 1702288. [\[CrossRef\]](#)
- Chen, C.; Jiang, Q.; Xu, H.; Zhang, Y.; Zhang, B.; Zhang, Z.; Lin, Z.; Zhang, S. Ni/SiO₂/Graphene-modified separator as a multifunctional polysulfide barrier for advanced lithium–sulfur batteries. *Nano Energy* **2020**, *76*, 105033. [\[CrossRef\]](#)
- Jiang, F.-N.; Yang, S.-J.; Cheng, X.-B.; Shi, P.; Ding, J.-F.; Chen, X.; Yuan, H.; Liu, L.; Huang, J.-Q.; Zhang, Q. Thermal safety of dendritic lithium against non-aqueous electrolyte in pouch-type lithium metal batteries. *J. Energy Chem.* **2022**, *72*, 158–165. [\[CrossRef\]](#)
- Zhang, B.; Wu, J.; Gu, J.; Li, S.; Yan, T.; Gao, X.-P. The Fundamental Understanding of Lithium Polysulfides in Ether-Based Electrolyte for Lithium–Sulfur Batteries. *ACS Energy Lett.* **2021**, *6*, 537–546. [\[CrossRef\]](#)
- Nie, Y.; Dai, X.; Wang, J.; Qian, Z.; Wang, Z.; Guo, H.; Yan, G.; Jiang, D.; Wang, R. Facile and scalable fabrication of lithophilic Cu O enables stable lithium metal anode. *J. Energy Chem.* **2022**, *75*, 285–292. [\[CrossRef\]](#)
- Feng, J.; Li, J.; Zhang, H.; Liu, W.; Lin, Z.; Wang, T.; Zhao, X.; Wang, F.; Song, J. Accelerating redox kinetics by ZIF-67 derived amorphous cobalt phosphide electrocatalyst for high-performance lithium–sulfur batteries. *Energy Mater.* **2023**, *3*, 4130122. [\[CrossRef\]](#)
- Liu, H.; Liu, X.; Li, W.; Guo, X.; Wang, Y.; Wang, G.; Zhao, D. Porous Carbon Composites for Next Generation Rechargeable Lithium Batteries. *Adv. Energy Mater.* **2017**, *7*, 1700283. [\[CrossRef\]](#)
- Xie, C.; Shan, H.; Song, X.; Chen, L.; Wang, J.; Shi, J.-W.; Hu, J.; Zhang, J.; Li, X. Flexible S@C-CNTs cathodes with robust mechanical strength via blade-coating for lithium–sulfur batteries. *J. Colloid Interface Sci.* **2021**, *592*, 448–454. [\[CrossRef\]](#) [\[PubMed\]](#)
- Li, S.; Chen, X.; Hu, F.; Zeng, R.; Huang, Y.; Yuan, L.; Xie, J. Cobalt-embedded carbon nanofiber as electrocatalyst for polysulfide redox reaction in lithium sulfur batteries. *Electrochim. Acta* **2019**, *304*, 11–19. [\[CrossRef\]](#)
- Wang, D.; Zhao, Z.-Y.; Wang, P.; Wang, S.-M.; Feng, M. Synthesis of MOF-derived nitrogen-doped carbon microtubules via template self-consumption. *Rare Met.* **2022**, *41*, 2582–2587. [\[CrossRef\]](#)
- Hou, L.-P.; Zhang, X.-Q.; Li, B.-Q.; Zhang, Q. Challenges and promises of lithium metal anode by soluble polysulfides in practical lithium–sulfur batteries. *Mater. Today* **2021**, *45*, 62–76. [\[CrossRef\]](#)
- Zhang, Y.; Wei, C.; Wu, M.-X.; Wang, Y.; Jiang, H.; Zhou, G.; Tang, X.; Liu, X. A high-performance COF-based aqueous zinc–bromine battery. *Chem. Eng. J.* **2023**, *451*, 138915–138925. [\[CrossRef\]](#)
- Wang, P.; Xi, B.; Huang, M.; Chen, W.; Feng, J.; Xiong, S. Emerging Catalysts to Promote Kinetics of Lithium–Sulfur Batteries. *Adv. Energy Mater.* **2021**, *11*, 2002893. [\[CrossRef\]](#)
- Liu, X.; Huang, J.Q.; Zhang, Q.; Mai, L. Nanostructured Metal Oxides and Sulfides for Lithium–Sulfur Batteries. *Adv. Mater.* **2017**, *29*, 1601759. [\[CrossRef\]](#)
- Liu, G.; Yuan, C.; Zeng, P.; Cheng, C.; Yan, T.; Dai, K.; Mao, J.; Zhang, L. Bidirectionally catalytic polysulfide conversion by high-conductive metal carbides for lithium–sulfur batteries. *J. Energy Chem.* **2022**, *67*, 73–81. [\[CrossRef\]](#)
- Yang, J.L.; Cai, D.Q.; Lin, Q.; Wang, X.Y.; Fang, Z.Q.; Huang, L.; Wang, Z.J.; Hao, X.G.; Zhao, S.X.; Li, J.; et al. Regulating the Li₂S deposition by grain boundaries in metal nitrides for stable lithium–sulfur batteries. *Nano Energy* **2022**, *91*, 106669. [\[CrossRef\]](#)

24. Zuo, J.-H.; Gong, Y.-J. Applications of transition-metal sulfides in the cathodes of lithium–sulfur batteries. *Tungsten* **2020**, *2*, 134–146. [CrossRef]
25. Tan, Z.; Li, H.; Feng, Q.; Jiang, L.; Pan, H.; Huang, Z.; Zhou, Q.; Zhou, H.; Ma, S.; Kuang, Y. One-pot synthesis of Fe/N/S-doped porous carbon nanotubes for efficient oxygen reduction reaction. *J. Mater. Chem. A* **2019**, *7*, 1607–1615. [CrossRef]
26. Li, J.; Zhang, H.; Luo, L.; Li, H.; He, J.; Zu, H.; Liu, L.; Wang, F.; Song, J. Blocking polysulfides with a Janus $\text{Fe}_3\text{C}/\text{N-CNF@RGO}$ electrode via physiochemical confinement and catalytic conversion for high-performance lithium–sulfur batteries. *J. Mater. Chem. A* **2021**, *9*, 2205–2213. [CrossRef]
27. Cao, Z.; Jia, J.; Chen, S.; Li, H.; Sang, M.; Yang, M.; Wang, X.; Yang, S. Integrating Polar and Conductive Fe_2O_3 - Fe_3C Interface with Rapid Polysulfide Diffusion and Conversion for High-Performance Lithium-Sulfur Batteries. *ACS Appl. Mater. Interfaces* **2019**, *11*, 39772–39781. [CrossRef] [PubMed]
28. Pan, H.; Tan, Z.; Zhou, H.; Jiang, L.; Huang, Z.; Feng, Q.; Zhou, Q.; Ma, S.; Kuang, Y. Fe_3C -N-doped carbon modified separator for high performance lithium-sulfur batteries. *J. Energy Chem.* **2019**, *39*, 101–108. [CrossRef]
29. Song, J.; Guo, X.; Zhang, J.; Chen, Y.; Zhang, C.; Luo, L.; Wang, F.; Wang, G. Rational design of free-standing 3D porous MXene/rGO hybrid aerogels as polysulfide reservoirs for high-energy lithium–sulfur batteries. *J. Mater. Chem. A* **2019**, *7*, 6507–6513. [CrossRef]
30. Li, J.; Song, J.; Luo, L.; Zhang, H.; Feng, J.; Zhao, X.; Guo, X.; Dong, H.; Chen, S.; Liu, H.; et al. Synergy of MXene with Se Infiltrated Porous N-Doped Carbon Nanofibers as Janus Electrodes for High-Performance So-dium/Lithium–Selenium Batteries. *Adv. Energy Mater.* **2022**, *12*, 2200894. [CrossRef]
31. Tan, Z.; Liu, S.; Zhang, X.; Wei, J.; Liu, Y.; Hou, L.; Yuan, C. Few-layered V_2C MXene derived 3D V_3S_4 nanocrystal functionalized carbon flakes boosting polysulfide adsorption and catalytic conversion towards Li–S batteries. *J. Mater. Chem. A* **2022**, *10*, 18679–18689. [CrossRef]
32. Zhang, C.; Feng, J.; Guo, X.; Zhang, J.; Zhang, W.; Zhang, L.; Song, J.; Shao, G.; Wang, G. Blocking polysulfide by physical confinement and catalytic conversion of SiO_2 @MXene for Li–S battery. *Appl. Phys. Lett.* **2023**, *122*, 193901–193907. [CrossRef]
33. Karimi, S.; Namazi, H. A photoluminescent folic acid-derived carbon dot functionalized magnetic dendrimer as a pH-responsive carrier for targeted doxorubicin delivery. *New J. Chem.* **2021**, *45*, 6397–6405. [CrossRef]
34. Ali, T.; Yan, C. 2 D Materials for Inhibiting the Shuttle Effect in Advanced Lithium–Sulfur Batteries. *Chemsuschem* **2020**, *13*, 1447–1479. [CrossRef] [PubMed]
35. Shi, C.; Song, J.; Zhang, Y.; Wang, X.; Jiang, Z.; Sun, T.; Zhao, J. Revealing the mechanisms of lithium-ion transport and conduction in composite solid polymer electrolytes. *Cell Rep. Phys. Sci.* **2023**, *4*, 101321–101337. [CrossRef]
36. Wang, X.; Sun, J.; Li, T.; Song, Z.; Wu, D.; Zhao, B.; Xiang, K.; Ai, W.; Fu, X.-Z.; Luo, J.-L. Folic acid self-assembly synthesis of ultrathin N-doped carbon nanosheets with single-atom metal catalysts. *Energy Storage Mater.* **2021**, *36*, 409–416. [CrossRef]
37. Yu, K.; Wang, X.; Yang, H.; Bai, Y.; Wu, C. Insight to defects regulation on sugarcane waste-derived hard carbon anode for sodi-um-ion batteries. *J. Energy Chem.* **2021**, *55*, 499–508. [CrossRef]
38. Zhang, Y.; Zhao, R.; Li, Y.; Zhu, X.; Zhang, B.; Lang, X.; Zhao, L.; Jin, B.; Zhu, Y.; Jiang, Q. Potassium-ion batteries with novel N, O enriched corn silk-derived carbon as anode exhibiting excellent rate performance. *J. Power Sources* **2021**, *481*, 228644. [CrossRef]
39. Wu, R.; Chen, S.; Deng, J.; Huang, X.; Song, Y.; Gan, R.; Wan, X.; Wei, Z. Hierarchically porous nitrogen-doped carbon as cathode for lithium–sulfur batteries. *J. Energy Chem.* **2018**, *27*, 1661–1667. [CrossRef]
40. Liu, Y.; Yang, C.; Li, Y.; Zheng, F.; Li, Y.; Deng, Q.; Zhong, W.; Wang, G.; Liu, T. FeSe_2 /nitrogen-doped carbon as anode material for Potassium-ion batteries. *Chem. Eng. J.* **2020**, *393*, 124590. [CrossRef]
41. Xiao, J.; Li, X.; Tang, K.; Wang, D.; Long, M.; Gao, H.; Chen, W.; Liu, C.; Liu, H.; Wang, G. Recent progress of emerging cathode materials for sodium ion batteries. *Mater. Chem. Front.* **2021**, *5*, 3735–3764. [CrossRef]
42. Zhou, Z.; Chen, Z.; Lv, H.; Zhao, Y.; Wei, H.; Huai, G.; Xu, R.; Wang, Y. High-entropy nanoparticle constructed porous honeycomb as a 3D sulfur host for lithium polysulfide adsorption and catalytic conversion in Li–S batteries. *J. Mater. Chem. A* **2023**, *11*, 5883–5894. [CrossRef]
43. Zhao, M.; Chen, X.; Li, X.; Li, B.; Huang, J. An Organodiselenide Comediator to Facilitate Sulfur Redox Kinetics in Lithium–Sulfur Batteries. *Adv. Mater.* **2021**, *33*, e2007298. [CrossRef] [PubMed]
44. Li, L.; Liu, H.; Jin, B.; Sheng, Q.; Li, Q.; Cui, M.; Li, Y.; Lang, X.; Jiang, Q. Functional Separator Modified with Reduced Graphene Oxide and Fe_3S_4 for High-Performance Lithium–Sulfur Batteries. *ACS Appl. Nano Mater.* **2023**, *6*, 1161–1170. [CrossRef]
45. Zhang, S.; Zhang, Y.; Ma, L.; Ma, C.; Zhang, C.; Chen, Y.; Chen, L.; Zhou, L.; Wei, W. Dual Active Sites of Oversaturated Fe-N(5) and Fe(2)O(3) Nanoparticles for Accelerating Redox Kinetics of Polysulfides. *Small* **2023**, *e2300293*. [CrossRef] [PubMed]
46. Huang, J.-Q.; Zhang, B.; Xu, Z.-L.; Abouali, S.; Akbari Garakani, M.; Huang, J.; Kim, J.-K. Novel interlayer made from Fe_3C /carbon nanofiber webs for high performance lithium–sulfur batteries. *J. Power Sources* **2015**, *285*, 43–50. [CrossRef]
47. Wang, S.; Liu, X.; Duan, H.; Deng, Y.; Chen, G. Fe_3C /Fe nanoparticles embedded in N-doped porous carbon nanosheets and graphene: A thin functional interlayer for PP separator to boost performance of Li–S batteries. *Chem. Eng. J.* **2021**, *415*, 129001. [CrossRef]
48. Wu, K.; Hu, Y.; Cheng, Z.; Pan, P.; Zhang, M.; Jiang, L.; Mao, J.; Ni, C.; Zhang, Y.; Wang, Z.; et al. Fe_3C composite carbon nanofiber interlayer for efficient trapping and conversion of polysulfides in lithium-sulfur batteries. *J. Alloy. Compd.* **2020**, *847*, 156447. [CrossRef]

49. Zhang, M.; Mu, J.; Li, Y.; Pan, Y.; Dong, Z.; Chen, B.; Guo, S.; Yuan, W.; Fang, H.; Hu, H.; et al. Propelling polysulfide redox by Fe3C-FeN heterostructure@nitrogen-doped carbon framework towards high-efficiency Li-S batteries. *J. Energy Chem.* **2023**, *78*, 105–114. [[CrossRef](#)]
50. Zhu, R.; Lin, S.; Jiao, J.; Ma, D.; Cai, Z.; Hany, K.; Hamouda, T.M.; Cai, Y. Magnetic and mesoporous Fe₃O₄-modified glass fiber separator for high-performance lithium-sulfur battery. *Ionics* **2019**, *26*, 2325–2334. [[CrossRef](#)]

Disclaimer/Publisher's Note: The statements, opinions and data contained in all publications are solely those of the individual author(s) and contributor(s) and not of MDPI and/or the editor(s). MDPI and/or the editor(s) disclaim responsibility for any injury to people or property resulting from any ideas, methods, instructions or products referred to in the content.